Evolution of Aerosol Size and Composition in the Indo-Gangetic Plain: Size-Resolved Analysis of High-Resolution Aerosol Mass Spectra

Navaneeth M. Thamban,[†] Bhuvana Joshi,[†] S. N. Tripathi,*[,†,‡] Donna Sueper,[§,∥]
Manjula R. Canagaratna,[§] Shamjad P. Moosakutty,[†] Rangu Satish,[⊥] and Neeraj Rastogi[⊥]

[†]Department of Civil Engineering, Indian Institute of Technology, Kanpur 208016, India

[‡]Centre for Environmental Science and Engineering, Indian Institute of Technology, Kanpur 208016, India

[§]Aerodyne Research, Inc., Billerica, Massachusetts 01821, United States

[∥]Cooperative Institute for Research in Environmental Sciences (CIRES), University of Colorado, Boulder, Colorado 80309, United States

[⊥]Geosciences Division, Physical Research Laboratory, Ahmedabad 380009, India

Ⓢ Supporting Information

ABSTRACT: This work highlights the first multiweek size-resolved analysis of high-resolution (HR) mass spectra from the Aerodyne aerosol mass spectrometer (AMS). High-resolution analysis allows for separation of isobaric interferences in the mass spectra and provides a more detailed view of the dynamic process by which both aerosol composition and size distribution change in the atmosphere. The data used in this analysis were obtained in the Indo-Gangetic Plain (IGP) during the winter of 2016 from 1 to 31 January. We report the temporal variations of particulate matter < 1 μm (PM$_1$) composition and link them to observed trends in chemically speciated particle size distributions. Organic and inorganic species are found to contribute on average to 54% and 46% of the aerosol mass, respectively, at the site. Positive matrix factorization (PMF) analysis of the organic HR-AMS spectra indicates that the primary organic aerosol sources are dominated by hydrocarbon-like organic aerosol (HOA) and biomass

burning organic aerosols (BBOA 1 and BBOA 2). Chloride-containing aerosol events that correlate with increases in BBOAs are also observed. Significant organic aerosol (OA) mass contributions are attributed to low volatile oxygenated organic aerosol, LV-OOA (37%), and biomass-influenced oxygenated organic aerosol, OOA-BBOA (21%). Average time trends in binned, speciated size distributions are estimated using individual high-resolution proxy ions or sums of ions that are most representative of the various aerosol species. The mean modal aerodynamic diameters (MMDs) of NO$_3^-$, SO$_4^{2-}$, NH$_{4+}$, and LV-OOA species are found to be greater than 600 nm and do not change significantly throughout the day. In contrast, primary organic aerosol (POA) particles such as HOA and BBOA show sharp diurnal trends in their MMDs. The average MMD of POA increases from ~375 nm in the morning to ~500 nm at midday, while a corresponding increase in MMD from ~450 to ~650 nm is observed for BBOA. Primary and secondary aerosol species have distinctive size distributions during the mornings and evenings, indicating that they are more externally mixed when primary sources are dominant. The size distributions of these species become more similar at midday within the time span of ~4 to 6 h when condensation of secondary oxidized organic aerosol likely results in rapid internal mixing and increasing degree of oxidation of aerosol species. The diurnal increases in MMDs correlate well with the diurnal increases in mass concentrations of LV-OOA. Taken together, the trends in size distributions and mass concentrations suggest that rapid particle growth due to condensation of photochemically produced secondary organic species is important in IGP even in the winter.

KEYWORDS: Biomass burning, Size distribution, High-resolution, Organics: India
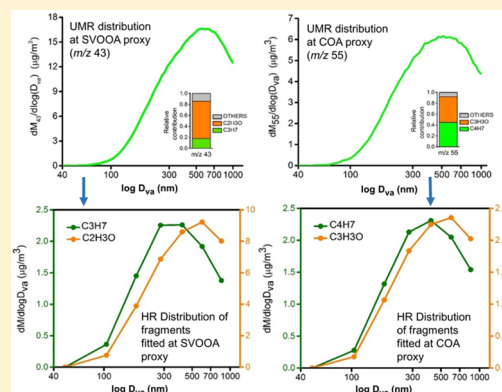
1. INTRODUCTION

Aerosols are known to affect the climate by altering the earth radiative budget by direct, semidirect, and indirect effects.[1−3] Among the aerosols, organic aerosols (OAs) are ubiquitous in the atmosphere and contribute to a significant fraction of fine aerosol mass.[4,5] Primary organic aerosols (POAs) are emitted

A

directly into the atmosphere, and secondary organic aerosols (SOAs) are formed by oxidation of precursors in the atmosphere. SOA species are less volatile and more hygroscopic.[4,6] Once formed in the atmosphere, SOAs can condense onto POAs and thus promote the internal mixing of secondary organic, and inorganic, species with POAs.[3] The chemical and morphological changes resulting from these condensation processes affect the size distribution of the aerosols and the atmospheric aging, cloud nucleating ability, radiative forcing interactions, and atmospheric lifetime.[7,8]

The sampling site for the present study is Kanpur, which is a highly populated industrial city located in the Indo-Gangetic Plain (IGP), a well-known aerosol hotspot in the world characterized by high aerosol loading.[9−11] Being located in the middle of the IGP, Kanpur receives aerosol loading both from local and long-range sources.[12] Especially during winter; the sampling site receives a significant fraction of regional biomass burning from the north and northwestern IGP.[13] These widespread (local and regional) biomass burnings and open trash burnings[11] along with emissions from coal power plants, vehicles, domestics cooking, brick kilns, and biofuel burning[9,12,14,15] generate heterogeneous aerosols that are very complex in characteristics.

Recent studies have found that a significant fraction of OAs in IGP are SOAs,[9,12,13,16] which promote their internal mixing.[17] However, the characterization of SOAs is challenging due to the complexity of their aging mechanism, composition, and sources.[6,18] The high-resolution time-of-flight aerosol mass spectrometer (termed "AMS" hereafter), manufactured by Aerodyne Research, Inc., is an instrument that is widely used for the physical and chemical characterization of sub-micrometer ambient aerosols in real time.[19,20] In the AMS, the vacuum aerodynamic diameters (D_{va}) of the nonrefractory sub-micrometer aerosols are derived from the particle velocities.[19,21] Mass-weighted size distributions of D_{va} of organics and inorganics have been reported in terms of their unit mass resolution (UMR) proxies,[22] which in turn can provide useful information about the evolution of aerosol particles in the atmosphere.[23]

While previous studies have identified unit mass resolution (UMR) proxies of various aerosol sources and processes,[20,23,24] these ions can have contributions from multiple interfering isobaric species in complex, polluted environments. High-resolution analysis of these UMR ions is then necessary to obtain a more unique ion proxy for the process or source of interest.

The key objective of this study is to utilize size-resolved high-resolution AMS mass spectra to understand the transformation processes of primary and secondary aerosol particles in IGP during the winter. The high-resolution analysis of the size-resolved spectra allows for a more direct comparison between the temporal and diurnal variations of ion size distributions and the trends in mass concentration of different organic factors extracted from the positive matrix factorization (PMF) analysis of the high-resolution mass spectra. According to our best understanding, this work highlights the first multiweek size-resolved analysis of high-resolution (HR) mass spectra from the AMS.

2. SITE DESCRIPTION AND INSTRUMENTATION

2.1. Sampling Site. The present study reports the real-time size distribution characteristics of nonrefractory aerosols measured during Jan. 1−31, 2016. The study was carried out at the Centre for Environmental Science and Engineering (CESE) building (26.5°N, 80.3°E, 142 m above mean sea level),

located in the Indian Institute of Technology—Kanpur (IIT-K) campus. The major sources of pollution at the sampling site are indoor and outdoor biomass burnings and vehicular and industrial emissions.[11,15] The study period is a winter season which is characterized by low temperatures (∼4 °C), high relative humidity (RH; up to 100%), and shallow boundary layer height, which favor the accumulation of pollutants.[12]

2.2. Instrumentation. The Aerodyne HR-ToF-AMS (AMS) was used to determine real-time physical and chemical characteristics of the nonrefractory aerosols in IGP. The nonrefractory species were measured by thermal heating (∼600 °C) followed by the electron ionization technique (70 eV) in AMS.[19] The time resolution of the data collection in AMS was set to 2 min, during which the operating mode was switched between mass spectrum (MS) mode and particle time-of-flight (PToF) mode. Since the collection efficiency of AMS can be affected by the RH of the ambient atmosphere,[25] the aerosols were dried before entering into AMS to an RH < 10% using a silica gel dryer. Ionization efficiency (IE) calibrations were done before, during, and after the sampling period. The calculated average relative ionization efficiency (RIE) value for NH_4^+ and NO_3^- were 4 and 1.1, respectively, during the sampling period. The assumed RIE values for SO_4^{2-}, Cl^-, and organics were 1.2, 1.3, and 1.4, respectively.[19]

Aerosol size distributions between 14 and 685 nm were measured using a scanning mobility particle sizer (SMPS, TSI 3696), which comprised a long differential mobility analyzer and a butanol based condensation particle counter (CPC, TS1 3775). In SMPS, the aerosols were segregated according to their mobility in a given electric field. A single particle soot photometer (SP2), manufactured by Droplet Measurement Technologies (DMT), was used to calculate the black carbon (BC) mass concentration at the sampling site. More details on the SP2 are described elsewhere.[26−29] Oxides of nitrogen (NO_x, i.e., $NO + NO_2$) and carbon monoxide (CO) were analyzed at 2 min integration time using gas analyzers (Serinus, Ecotech), which work on the principles of chemiluminescence and NDIR technique.

3. METHODS

3.1. Data Analysis. Unit mass resolution and high-resolution data analyses were performed on the AMS data[19] by using Squirrel (Version 1.60) and PIKA (Version 1.20), respectively. AMS size distributions were derived from PToF mode measurements, and ensemble size distributions of aerosol species were obtained by summing the size distributions of all ions belonging to that species. During UMR size distribution estimation, two "DC regions" were selected to remove the background ion signal where the particle velocity is too low or high to be transmitted in AMS.[30] The PToF length and duty cycle of the chopper were 0.295 m and 2%, respectively. The AMS size calibration was performed with ammonium nitrate (Supporting Information Figure S10). The HR analysis was performed using PIKA, with the high-resolution peak fitting of mass spectra (MS) performed.[20]

AMS mass concentrations were calculated using a constant collection efficiency of 0.5 for all species.[9,19,31,32] In addition, the application of this collection efficiency showed good agreement between the mass concentrations of AMS and SMPS in the sampling site.[13] Adjustments on the standard air fragmentation table were performed for air peaks such as 16 (O^+), 29 ($N_{15}N^+$), and 44 (CO_2^+) by using background mass spectra obtained while sampling through a HEPA filter.[9,13] Elemental ratios of the

PMF factors were obtained from the high-resolution mass spectra using the methods originally proposed by Aiken et al.[33] and updated by Canagaratna et al.[34]

3.2. HR-PToF Size Distribution Estimation.

In this work, size-dependent analysis of high-resolution AMS mass spectra is referred to as HR-PToF analysis for simplicity. For each 2 min run in AMS, 50% time was spent in each MS and PToF mode. After the field campaign concluded, raw data files were averaged to 3 h to increase the signal-to-noise ratio for HR peak fitting and to speed up data processing. HR-PToF analysis was performed on this 3 h averaged AMS high-resolution mass spectra (PIKA, Version 1.20). The PToF data files are indexed along with MS data, and the raw mass spectra measured in the particle time-of-flight (PToF) mode were processed by assuming the same peak-fitting parameters (HR peak shape, HR peak width, and m/z calibration) as used when analyzing the MS mode. The same HR ions were fitted between PToF and MS data.

The entire PToF range was grouped into 10 equally spaced particle time-of-flight bins. The set of 10 PToF bins have vacuum aerodynamic diameter (D_{va}) values that increase exponentially with PToF time. The geometric mean of the D_{va} values of a particular HR-PToF sized bin was used to represent that bin and is termed as the mean bin diameter (hereafter termed as MBD). The PToF grouping step resulted in 7 new bins, bin nos. 4−10, with MBD ranging from ∼49 to 853 nm (Table S1). The PToF bin groupings represented by bin nos. 0−3 were not used in the present study since the aerodynamic lens has negligible transmission for particles in this size range[35] and the size calibration did not extend to this region.

PToF analysis of UMR data requires an estimate of the background via the selection of one or two DC regions, one at smaller ("DC region 1") and the other at higher ("DC region 2") PToF time due to overlapping signal contributions from nominal gas and particle fragments, such as $^{15}N^+$ from air and NH^+ from ammonium aerosol at m/z 15.[30] The choice of the DC regions for PToF UMR analysis is optimally the lowest average region in the PToF time domain. The HR analysis results in the separation of signals between nominal fragments of predominately air and aerosol origin such as the $^{15}N^+$ and NH^+ examples. However, in the case of the CO_2^+ fragment at m/z 44, significant PToF signal can result from both the gas and the aerosol phases. The choice of background for all HR ions was determined by examining the relative minima in the PToF time domain for the CO_2^+ signal, which corresponded to bin 4, with an estimated D_{va} of 33−74 nm. Selecting this bin can cause an overestimation of the background for gas phase ions or for a signal from very small particles which reached the detector. The potential overestimation does not impact any results of the relative changes across the different size bins. For this experimental setup, the relative minima in the PToF domain for any ion fragment was never at the largest PToF times recorded, with the exception of purely gas phase ions such as N_2^+.

The difference between the high-resolution mass spectra observed at higher bins (bin nos. 5−10) and bin no. 4 was used to calculate background-subtracted HR-PToF mass spectra and signal intensities for each HR-PToF size bin. The temporal variations of the modes of the HR size distributions were further used to calculate the mean modal diameter (MMD) of that particular HR species. MMD is the mean of the modes of HR size distribution at a particular period.

3.3. Positive Matrix Factorization (PMF) of OA.

Positive matrix factorization (PMF)[36] was performed on the 2 min averaged HR V-mode organics data (m/z 12−150, no organics ions excluded) by using the PMF evaluation tool (PET, Version 2.06)[37] to understand the sources of OA at this site.[9,11,13] PMF analysis of the HR-AMS OA mass spectra resulted in the identification of various primary and secondary factors including low volatile oxygenated OA (LV-OOA), two biomass burning OA factors (BBOA 1 and BBOA 2), BBOA-influenced aged OA (OOA-BBOA), and hydrocarbon-like OA (HOA). A five-factor PMF solution is identified based on the residuals (Figure S1), physical interpretability (Figure S2), and the correlation with internal and external factors (Figures S3 and S6−S8).[37]

In PMF, the observed data (defined as a bilinear factor model) are resolved with the least-squares fitting method that minimizes Q, which is the sum over all data points of the ratios between the squares of the fit residuals and error estimates at each data point. The rotational forcing parameter values (f_{peak}) were varied from −5 to +5 (with an interval of 0.5) during the PMF analysis. Q/Q_{exp} values refer to the ratios between Q, i.e., the actual sum of squares of the scaled residuals acquired from the PMF least-squares fit, and the ideal $Q/(Q_{exp})$ acquired if the fit residuals at each point were equal to the noise specified for each data point.[37]

We have selected a five-factor PMF solution; selection details are shown in Figure S1a−f. In Figure S1a, Q/Q_{exp} values decrease from 23 (1 factor) to 4.5 (10 factors), which indicates that the additional factors explain the data variation more clearly.[37] The largest reduction in Q/Q_{exp} value is observed when up to 5 factors are added, and then the Q/Q_{exp} value is observed to plateau for larger factor numbers (Figure S1). The five-factor solution was chosen based on a comparison of the residual spectra and time series between the factors (Figure S4), interpretability of the spectra and the correlation of the factors with AMS spectral tracers and external tracers (Figures S2 and S3).[37] The 5 factor solution provided a better tracer correlation than the factor 4 solution, and higher factor solutions did not provide any new interpretable information. The pie chart in Figure S2 shows the relative contribution of each factor.

Although the 5 factor solution was chosen from this analysis, it is useful to note that the Q/Q_{exp} value observed for this solution is higher than the ideal value of 1. The high Q/Q_{exp} values (Figure S1b,e,f) in the 5 factor PMF solution reflects the difficulty in separating the complex and mixed POA and SOA sources from each other in the winter. This is consistent with the fact that the scaled residuals as a function of time have peaks that are very sharp and that the scaled residuals as a function of m/z are highest for the levoglucosan ions (mainly at m/z 60), which are proxies for BBOA (Figure S1c,f). Additionally, higher source variability in a region heavily influenced by disparate burning sources likely make it difficult to extract a single BBOA factor in the PMF solution. The correlation between previously identified high-resolution AMS organic proxy ions ($C_2H_3O^+$, $C_2H_4O_2^+$, $C_3H_5O_2^+$, $C_4H_9^+$, $C_4H_7^+$, and CO_2^+), inorganic (NO_3^-, SO_4^{2-}) ions, external gaseous tracers (carbon monoxide and nitrogen oxides) and black carbon with the PMF factors are shown in Figure S3. See also Figures S6, S7, and S8.

The HOA factor is a primary vehicular OA emission and is correlated well with external factors, such as BC ($R^2 = 0.71$), NO_x ($R^2 = 0.64$), CO ($R^2 = 0.68$), and with AMS derived $C_4H_9^+$ ($R^2 = 0.73$) concentrations. The LV-OOA factor is identified on the basis of the high intensity of CO_2^+ in its factor MS, and its diurnal cycle, which shows significant production during the daytime despite increased boundary layer heights. LV-OOA factor is a highly oxygenated factor (O/C = 0.91), which

correlated positively with SO_4^{2-} ($R^2 = 0.30$) and CO_2^+ ($R^2 = 0.51$).

As described above and shown in Figure S1c,f, the levoglucosan fragments related to BBOA dominate the highest Q/Q_{exp} contributions, and these residuals occur episodically in time. This is likely due to the fact that a single BBOA factor does not provide a good representation of the multiple distinct burning events with different mass spectra that are sampled during this campaign. In this analysis, 3 factors with levoglucosan fragments, i.e., $C_2H_4O_2^+$ and $C_3H_5O_2^+$,[24,31,38] were observed and are named according to their correlation coefficients with these fragments. BBOA 1 has the highest correlation, while BBOA 2 has a lower correlation. The low correlation of BBOA 2 with trace gases of vehicle emission (Figure S7) and high O/C ratio (O/C = 0.37) indicate that the BBOA 2 factor is not highly influenced from vehicular emissions. A third factor, OOA-BBOA, is a mixed factor whose MS is dominated by oxidized organic marker fragments (CO_2^+) but is still influenced by BBOA. This factor is positively correlated with secondary organic (CO_2^+ ($R^2 = 0.63$)), inorganic (SO_4^{2-} ($R^2 = 0.38$)), and BBOA proxies (i.e., $C_2H_4O_2^+$ ($R^2 = 0.35$) and $C_3H_5O_2^+$ ($R^2 = 0.43$)). The positive correlation between CO_2^+ with $C_2H_4O_2^+$ and $C_3H_5O_2^+$ ($R^2 = 0.28$ and 0.41, respectively), shown in Figure S6, indicate that aged BBOA-influenced aerosols also contribute toward some of the observed OOA. Mixed factors similar to OOA-BBOA were present in previous PMF studies also in the sampling site.[9,12,13,16] To understand the mixed factors due to the rotational ambiguity, different f_{peak} values were tried during the PMF analysis. However, the different f_{peak} values did not provide a clearer separation of the OOA and BBOA from each other. Future studies with the help of an ME-2[39] engine may give a better representation of BBOA factors in this sampling site.

Figure S8 shows the strong correlation ($R^2 = 0.81$) between the levoglucosan fragment $C_2H_4O_2^+$ and the chloride species. This indicates that chloride-containing species are co-emitted with burning. Figure S9 shows the correlation of measured and predicted NH_4^+ and their relation to the high-chloride events in Figure 1g. The fact that the events with the highest chloride concentrations are not fully neutralized suggests that the chloride that is emitted during these events is not solely in the form of NH_4Cl.

The highly oxygenated LV-OOA factor (O/C = 0.91) and the less oxidized biomass-influenced OOA-BBOA factor (O/C = 0.73) are generally associated with SOA.[40] HOA is a primary factor (O/C = 0.25) with the clear signature of hydrocarbon species.[40] BBOA 1 factor (O/C = 0.21) is a primary biomass burning factor. The mass spectrum of BBOA 1 is similar to that of the oxygenated primary organic aerosol (OPOA) factor identified in the previous studies from the same site,[16,17] but with specific levoglucosan peaks at m/z 60 and 73 and a higher relative contribution from primary fragments. BBOA 2 (O/C = 0.37) is a biomass burning factor with slightly higher O/C than that of BBOA 1 and also that is consistent with BBOA components observed in other ambient environments such as Mexico city, i.e., 0.30−0.45.[41]

4. RESULTS AND DISCUSSION

4.1. Temporal Variation of the PM_1 Nonrefractory Species.
The temporal characteristics of the mass and size distributions of the nonrefractory aerosols in IGP during the sampling period are shown in Figure 1a−h. As reported from previous studies,[9,11−13,42] organics constitute the major mass
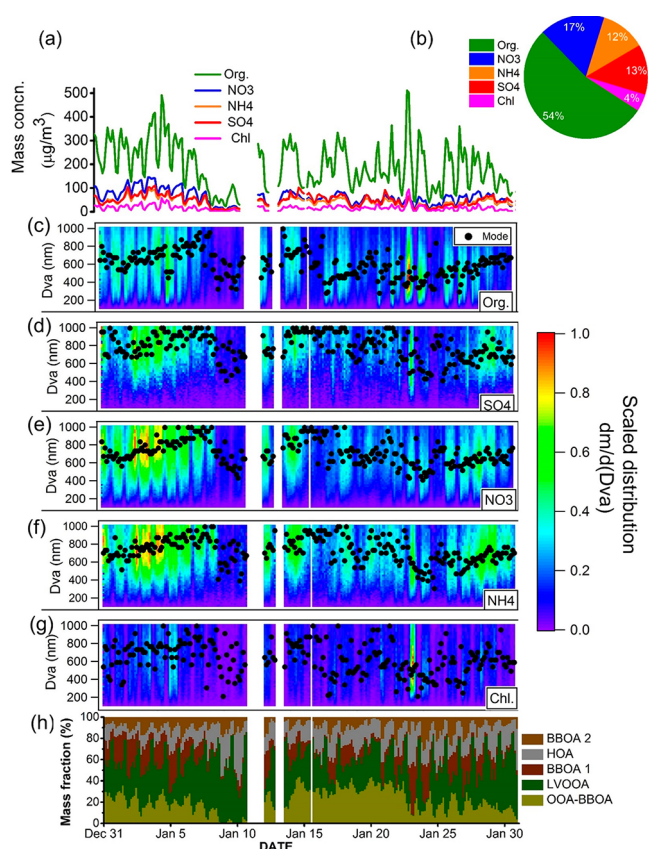

Figure 1. Temporal variations of the mass concentrations (a), nonrefractory PM_1 composition (b), size distributions of the PM_1 nonrefractory species (c−g), and mass fraction of PMF factors (h).

fraction of the PM_1, i.e., 54%, followed by nitrate, sulfate, and ammonium (12−17%), during the sampling period in IGP (Figure 1b). The temporal variation in the fractional contribution of PMF factors toward the total organic mass concentration is shown in Figure 1h. Two distinct high aerosol loading events on January 5 and 24 were observed and are characterized by a high mass fraction of POA, which for these data are represented by HOA, BBOA 1, and BBOA 2.

Panels c−g of Figure 1 show the image plots of the size distributions obtained from UMR analysis of the AMS PToF data. In UMR size distribution analysis, the change in the mode of the UMR size distribution of organics and inorganics (ammonium, nitrate, chloride, and sulfate) are shown as a function of time. The color scale of the time-dependent bin-wise concentration of all of these species is scaled from 0 to 1 to more clearly visualize the relative changes in size distributions of the respective species.

In general, the variation in aerosol composition and speciated size distributions can be classified according to different time periods. During the period before January 10, the aerosol species show clear diurnal cycles and the modes of all of the particle size distributions are similar to each other with a clear increase in mode size from around 600 to 800 nm over the 10 days. This particular period also shows a high background concentration of nitrate (NO_3^-), ammonium (NH_4^+), and sulfate (SO_4^{2-}) with a higher mass fraction of oxidized secondary PMF factors (LV-OOA + OOA-BBOA). The larger size distributions of the secondary organic and inorganic species in the earlier sampling period suggest that these aerosols are aged during this period. The period between January 17 and January 24 is characterized
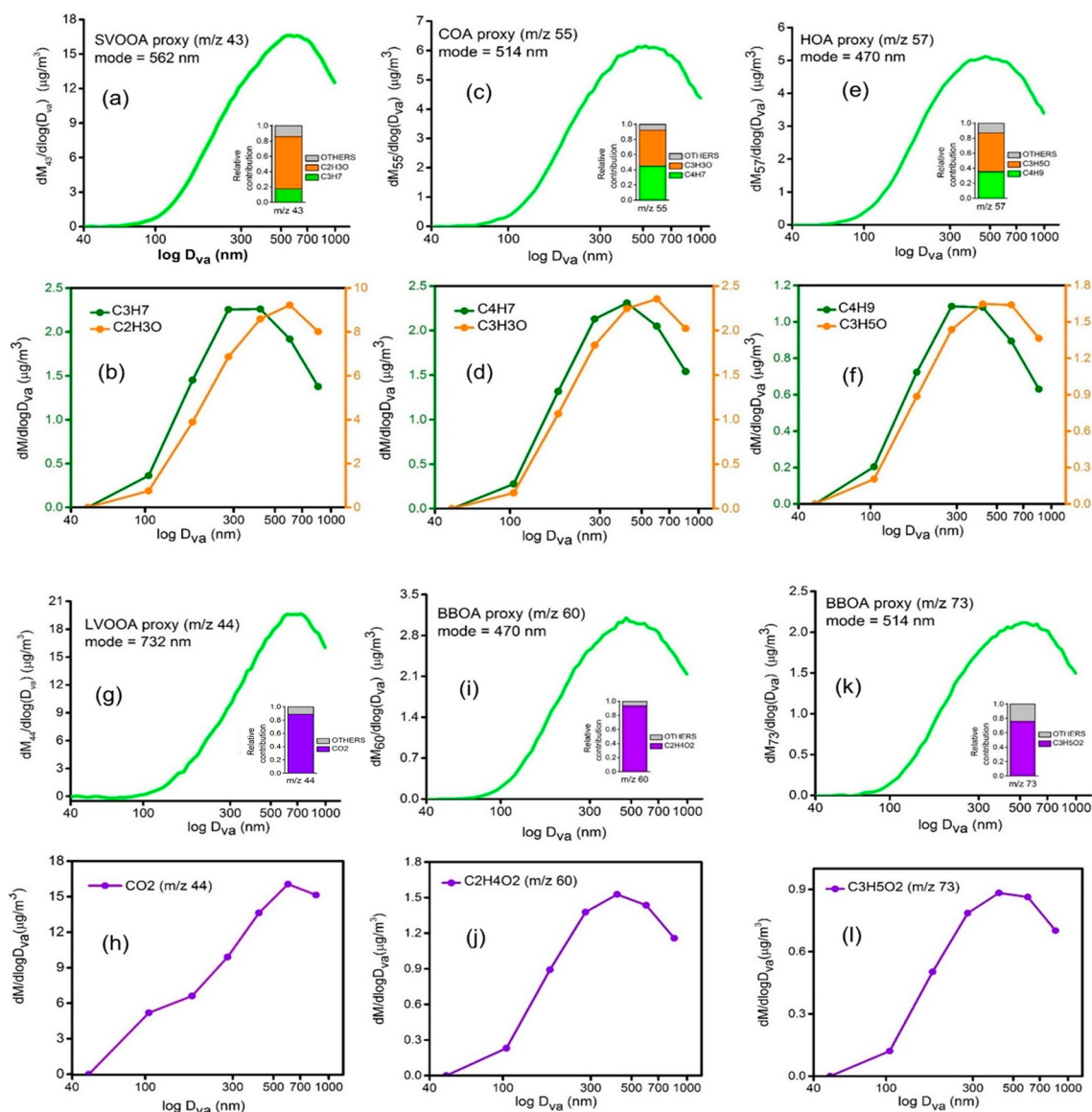
Figure 2. UMR size distributions of (a) SVOOA (m/z 43), (c) COA (m/z 55), and (e) HOA (m/z 57) proxies (top row) and the respective binned HR size distributions (b, d, and f) of ions (second row). The third and bottom rows indicate the UMR size distributions of LVOOA (m/z 44) (g) and BBOA proxies (m/z 60 (i) and m/z 73 (k)) and the corresponding binned HR size distribution of CO_2^+ (h), $C_2H_4O_2^+$ (j) and $C_3H_5O_2^+$ (l) during the sampling period. The y-axes of panels a–l are nitrate equivalent mass concentrations.

by reduced diurnal behavior of inorganic species and distinct increase in the LV-OOA (Figure S11) in midday. The size distributions of the inorganic species during this time have large size modes (around 800 nm), while the mode of the organic size distribution is significantly smaller (400−600 nm).

The smaller organic size distributions are consistent with the increased contribution of the HOA, BBOA 1, and BBOA 2 components during this time. The distinct modes in the organic and inorganic size distributions indicate a more externally mixed aerosol during this time. During the period after January 24, diurnal behavior in the speciated mass concentrations is observed again, but the background concentrations of all of the species are lower than in the period before January 10. The particle size distributions of all of the species are also generally smaller (600 nm) and similar across the species, suggestive of a more internally mixed aerosol.

As shown in Figure S2, LV-OOA is the dominant OA component and shows a strong diurnal trend on most days

(Figure 1h). The smallest modes in the organic size distribution are observed during the high loading events on January 5 and 24 that have a higher mass fraction of POA factors. These events also show an increased presence of a similar lower aerosol mode that contains chloride. The mass concentration of Cl⁻ is correlated well with that of the BBOA fragment ($C_2H_4O_2^+$), $R^2 =$ 0.82 (Figure S8). While a portion of Cl⁻ is present as NH_4Cl (Figure S9) in the sampling site, Cl⁻ is not completely neutralized during the events that correlate with biomass burning. The simultaneous observation of small organics (dominated by BBOA-1 and BBOA-2 factors) and Cl⁻-containing particles suggests that they are co-emitted potentially from sources such as local trash or garbage burning in addition to their presence as NH_4Cl in the sampling site.

4.2. HR Size Distributions of Organic Proxies. Previous studies have identified several UMR organic proxies. These proxies include SVOOA (m/z 43),[43] COA (m/z 55),[24] HOA (m/z 57), LV-OOA (m/z 44),[23] and BBOA (m/z 60 and m/z

73).[4,33] Figure 2, which compares the UMR and HR analysis of the PToF mode data at these proxies, shows the degree to which the UMR size distributions observed for the various organic proxies are biased by the relative contributions from isobaric species that have different sources and processes. The size distribution of various UMR proxies are shown along with the relative contributions of HR species that contribute to the UMR ion signal in the top and third row panels of Figure 2. The second and bottom row panels in Figure 2 show the size distributions of the high-resolution ions that contribute to the UMR ion. The HR size distributions have fewer points than the UMR size distributions as they are calculated by averaging over wider size bins (10 total bins vs 80 bins).

The high-resolution peak fitting of the SVOOA proxy (m/z 43) shows both primary ($C_3H_7^+$) and secondary ($C_2H_3O^+$) organic fragments, which contribute ≈20% and 70%, respectively, toward the mean mass of SVOOA proxy. $C_3H_7^+$ is a hydrocarbon-rich fragment, which is likely a signature of POA emitted from meat cooking, engine exhaust, and plastic burning.[24] $C_2H_3O^+$, on the other hand, is typically observed from non-acid oxygenates and is a dominant secondary organic fragment in OOA components observed in the atmosphere.[40]

The HR-PToF mass distribution of SVOOA proxy shows distinct modes for $C_3H_7^+$ and $C_2H_3O^+$. While the $C_3H_7^+$ distribution peaks between 281 and 417 nm, $C_2H_3O^+$ distribution shows a distinct peak at 600 nm (Figure 2b). The difference in the distribution patterns of the isobaric, but chemically distinct, oxygen- and non-oxygen-containing fragments are also observed at COA (m/z 55) and HOA (m/z 57) proxies. The UMR size distributions of COA and HOA proxies may be more sensitive to the variation in the mass fractions of the oxygen- and non-oxygen-containing fragments, since the isobaric species have a contribution almost equal to that of the proxy ion of interest (Figure 2c,e). The COA proxy is mainly composed of $C_4H_7^+$ (Figure 2d) and $C_3H_3O^+$ (Figure 2d) fragments,[44] which contribute approximately 45% and 50% toward the mass observed at the UMR COA proxy. The mode of $C_4H_7^+$ size distribution is located at 417 nm, with a significant contribution from lower bins. In the case of $C_3H_3O^+$, the mode of the distribution is shifted toward 600 nm, with a decreased contribution at lower diameter (281 nm) and an increased contribution at higher diameter (853 nm).

The HOA UMR proxy (m/z 57) contains the hydrocarbon ($C_4H_9^+$) and oxygen-containing ($C_3H_5O^+$) fragments with relative contributions of ≈38% and 50%, respectively, toward the mass of the HOA proxy. In the case of $C_4H_9^+$, the size distribution is broad with a peak between 286 and 417 nm, while the oxygenated $C_3H_5O^+$ fragment peaks at a larger size around 600 nm (Figure 2f). Even though the modes of the UMR size distributions of SVOOA, COA, and HOA proxies (Figure 2a,c,e, respectively) are located in a narrow range of diameters, i.e., 470−562 nm, the HR size distributions of the hydrocarbon and oxygen-containing fragments in these proxies show a distinct distribution pattern. The hydrocarbon fragments at these UMR proxies are observed to have size distributions that peak at lower diameters, while the oxygen-containing fragments have size distributions that peak at higher diameters. As shown in Figure S13 of the Supporting Information, this trend appears to be general and is observed across all hydrocarbon and oxygenated fragments in the AMS spectrum. These observations are consistent with previous work by Zhang et al.[45] and Mohr et al.,[44] which have shown that the size distribution of the HOA and COA UMR proxies, which are dominated by hydrocarbon

fragments, peak at smaller diameters than OOA, which is characterized by oxygen-containing fragments.

HR-PToF size distributions at the UMR proxies of LV-OOA (m/z 44) and BBOA (m/z 60 and 73) are shown in Figure 2g−l. The HR distribution mode of CO_2^+ (Figure 2h) peaks around 600 nm with a notable mass concentration that is still observed at higher diameter, i.e., 853 nm. BBOA is identified by the characteristic mass fragments of levoglucosan at m/z 60 and 73, i.e., $C_2H_4O_2^+$ and $C_3H_5O_2^+$, respectively.[31,44] Both $C_2H_4O_2^+$ and $C_3H_5O_2^+$ contribute significantly, i.e., 95% and 80%, respectively (Figure 2i,k, respectively) toward the signal of the BBOA proxies at m/z 60 and 73. Both these BBOA fragments ($C_2H_4O_2^+$ and $C_3H_5O_2^+$) show a similar size distribution pattern with a peak around 417 nm (Figure 2j,l, respectively).

4.3. Diurnal Variations of Mass and MBD of HR Organic Families and Inorganics Species. Figure 3 shows the 3 h
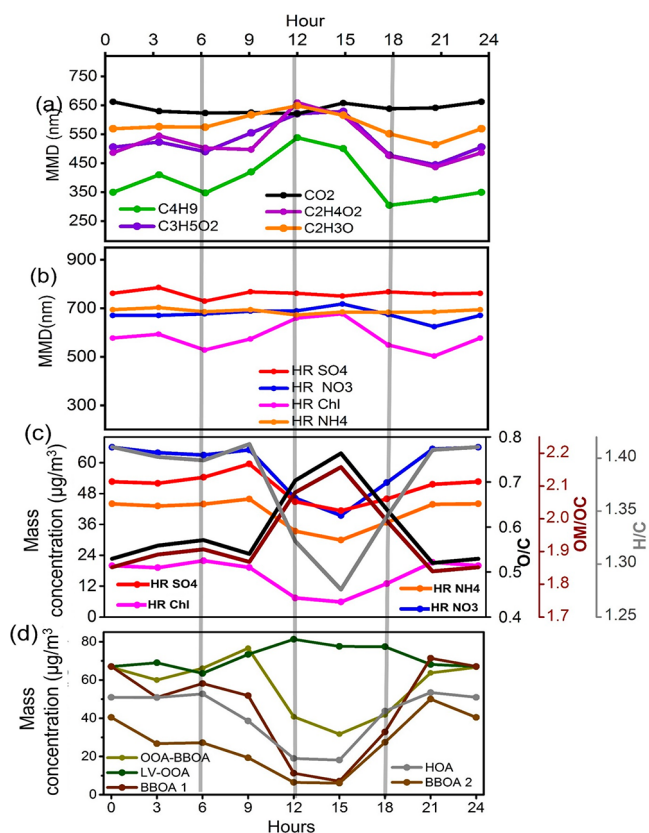

Figure 3. Diurnal variation of the mass and MMD of HR organics and inorganics proxy species. Whiskers in panels a and b indicate standard deviation in the average diameters during the sampling period. The diurnal variation of the mass concentration of inorganics and organics proxies are indicated in panels c and d.

averaged diurnal variations in the MMDs of the typical HR ion proxies of organic and inorganic species along with the diurnal mass concentrations of the inorganic species and organic PMF factors. The HR organic ion proxies for BBOA ($C_2H_4O_2^+$ and $C_3H_5O_2^+$), HOA ($C_4H_9^+$), SV-OOA ($C_2H_3O^+$), and LV-OOA (CO_2^+) are shown in Figure 3a. As shown in Figure 3d, the mass contributions of primary emissions from HOA and BBOA are largest in the evening and night when the boundary layer is low and primary emissions are high. Secondary aerosol contributions are important throughout the day, with OOA species becoming particularly dominant at midday when photochemistry is high.

Daily production in OOA species has been reported in many urban environments.[33] This increase in LV-OOA concentration and O/C ratio at daytime indicates that the local photochemical production dominates over the increase in the boundary layer height in the afternoon.[13,46]

Figure 3a shows that both of the HR ion proxies of BBOA have very similar diurnal trends in MMDs with smaller sizes being observed when the mass concentrations of primary emissions are high and larger MMDs at midday. The MMD of the HOA tracer is smaller than those of the BBOA tracers, consistent with previous measurements that have shown that freshly emitted BBOA particles are larger than HOA particles in size.[44] It is useful to note, however, that while fresh HOA from water pump engine exhaust[47] and vehicle sources[48] and in ambient environments[31,33] is typically observed to have a $D_{va} \sim$ 100 nm[23,47,48] in the AMS due to its fractal nature, the morning MMD observed for $C_4H_9^+$ is $D_{va} \sim 350$ nm. This indicates that either the HOA is coated enough to become more spherical or that at this site the $C_4H_9^+$ ion, which is also a significant fragment from BBOA species, reflects the average behavior in the size distribution of primary organic aerosols (POAs) rather than the behavior of HOA alone. This higher MMD of HOA can also be correlated with the idling of the vehicles that could relatively increase the size distribution of HOA toward higher bins.[47,49]

A key observation in Figure 3a is that MMDs of the POA signature ions show significant growth during the day. Small daytime increases in diameter are also observed for the SV-OOA proxy $C_2H_3O^+$. The growth in these particles is observed at around the same time as the increase in secondary LV-OOA and the accompanying increase in OM/OC and O/C (Figure 3c) of the measured organic aerosol. This indicates that condensation of OOA, particularly LV-OOA, is an important contributor to the growth of POAs in this region. It is also important to note that the changes in the density and shape of the condensing surface during LV-OOA condensation can further increase the MMDs of the primary species such as HOA.[21,50]

Since condensation of gas phase species is driven by the available particle surface area, it is useful to examine the number, area, and volume-weighted size distributions measured at the site with the SMPS (Figure S5). It is observed that the mode of the number and surface area distribution is shifting toward higher diameters during midday (Figure S5a). The relative shift in the distribution toward the higher bins can also be seen in Figure S5b–d, indicating the growth of the particles at midday in the sampling site.

The increase in particle MMD could be due to several processes including coagulation, condensation, and volatilization of primary aerosol species that recondense onto the available condensation sink. Previous studies have shown that the concentration of condensable species in polluted cities such as Kanpur[51] and Delhi[52] is significantly higher than that in a pristine environment. Moreover, the large contribution of anthropogenic emissions in these locations also results in a high condensation sink that is favorable to condensation. In Kanpur, for example, the condensation sink from pre-existing large particles has been shown to suppress particle nucleation.[51] On the basis of these studies, condensation of OOA is likely to be a dominant source for the growth of particle MMD at midday in this location. A study using "dynamic models" is required,[51−56] however, to obtain a more detailed understanding of the mechanisms that lead to the observed particle growth.

The mode of the surface area distribution is at a mobility diameter of 300 nm (Figure S12), which corresponds to a D_{va} of

435 nm for nonrefractory species. The latter value is calculated by assuming a spherical particle and calculating the particle density of 1.45 g cm^{-3} based on the combined inorganic and organic particle composition derived from the AMS by assuming the densities mentioned in Salcedo et al.,[57] i.e., 1.75 g cm^{-3} for ammonium, nitrate, and sulfate, 1.52 g cm^{-3} for chloride, and 1.2 g cm^{-3} for organics.

The fact that the largest change in MMDs is observed for particles with D_{va} values that correspond to the mode of the surface area distribution supports the idea that condensational growth is a primary source for the observed trends in MMD. Figure 3b shows that the MMD of aerosol particles that contain Cl$^-$ species also show a diurnal increase during the day. As discussed earlier, some of the Cl$^-$-containing ions are likely associated with primary aerosol species that are co-emitted from heterogeneous sources such as coal combustion, residential burning, and garbage burning.[58,59] The Cl$^-$ species MMD is slightly higher than those of the BBOA tracers. This may indicate that while these species are co-emitted, they are not fully internally mixed. The growth observed in the MMD of Cl$^-$-containing aerosol particles does follow the same diurnal trend as that observed for primary organic species, however, suggesting that condensation of OOA species onto the Cl$^-$-containing particles is important for the growth of these particles as well.

5. ENVIRONMENTAL IMPLICATION

During winter, IGP receives aerosols with complex characteristics in origin and age. Among the PM$_1$ aerosols, organic species contribute a major mass fraction (54%). The variability in the size of the organic aerosols indicates heterogeneity in their sources in IGP. However, BBOA-, LV-OOA-, and HOA-influenced OA sources dominate. The present study utilizes size-resolved analysis of high-resolution AMS spectra to investigate the evolution of particle size distribution in the atmosphere in more detail. Distinct externally mixed primary and secondary aerosol particles are observed in the mornings, evenings, and nights when photochemistry does not take place. At midday when photochemical activity is high, however, diurnal growth of primary particles due to condensation of secondary oxidized organic species is observed. Condensation dominated growth is observed to occur on the time scale of a few hours. This indicates that despite the many different sources of aerosol that are present at this site, condensation dominated growth results in efficient internal mixing of aerosol species during the day and in rapid changes of the average particle composition. Models of ambient aerosol in IGP will need to take these changes in size and temporally resolved particle composition into account in order to accurately predict their evolution and effects in the atmosphere.

■ ASSOCIATED CONTENT

Ⓢ Supporting Information

The Supporting Information is available free of charge on the ACS Publications website at DOI: 10.1021/acsearthspace-chem.8b00207.

> Details of five-factor PMF solution in HR-PMF analysis (Figure S1); source profiles of OA factors and their relative contributions (Figure S2); correlation of PMF factors (Figure S3); details of the residuals in the time series and PMF solution profiles (Figure S4); diurnal variation in the number concentration and the mean

modal diameter and diurnal variations of number, surface area, and volume distribution (Figure S5); correlation plots of CO_2^+ (Figure S6), of BBOA 2 factor (Figure S7), of $C_2H_4O_2^+$ and chloride (Figure S8), and of predicated and measured NH_4^+ concentrations (Figure S9); size calibration curve (Figure S10); diurnal mass concentrations (Figure S11); SMPS derived surface area distributions (Figure S12); HR-PToF distribution of primary and secondary organic families (Figure S13); details of the binning of HR-PToF size distribution calculation (Table S1) (PDF)

■ AUTHOR INFORMATION

Corresponding Author
*E-mail: snt@iitk.ac.in.

ORCID ⦿
Navaneeth M. Thamban: 0000-0002-9370-0211
S. N. Tripathi: 0000-0002-6402-4680
Shamjad P. Moosakutty: 0000-0002-1955-6661
Rangu Satish: 0000-0002-5764-0231
Neeraj Rastogi: 0000-0003-4532-7827

Notes
The authors declare no competing financial interest.

■ REFERENCES

(1) IPCC, 2001. In *Climate Change 2001: The Scientific Basis. Contribution of Working Group 1 to the Third Assessment Report of the Intergovenmental Panle on Climate Change*; Houghton, J. T., Ding, Y., Griggs, D. J., Noguer, M., van der Linden, P. J., Dai, X.., Maskell, K., Johnson, C. A., Eds.; Cambridge University Press: Cambridge, U.K., 2001.

(2) Albrecht, B. A. Aerosols, Cloud Microphysics, and Fractional Cloudiness. *Science (Washington, DC, U. S.)* **1989**, *245* (4923), 1227−1230.

(3) Jacobson, M. Z. Strong Radiative Heating Due to the Mixing State of Black Carbon in Atmospheric Aerosols. *Nature* **2001**, *409* (6821), 695−697.

(4) Jimenez, J. L.; Canagaratna, M. R.; Donahue, N. M.; Prevot, A. S. H.; Zhang, Q.; Kroll, J. H.; DeCarlo, P. F.; Allan, J. D.; Coe, H.; Ng, N. L.; et al. Evolution of Organic Aerosols in the Atmosphere. *Science (Washington, DC, U. S.)* **2009**, *326* (5959), 1525−1529.

(5) Zhang, Q.; Jimenez, J. L.; Canagaratna, M. R.; Allan, J. D.; Coe, H.; Ulbrich, I.; Alfarra, M. R.; Takami, A.; Middlebrook, A. M.; Sun, Y. L.; et al. Ubiquity and Dominance of Oxygenated Species in Organic Aerosols in Anthropogenically-Influenced Northern Hemisphere Midlatitudes. *Geophys. Res. Lett.* **2007**, *34* (13), L13801.

(6) Hallquist, M.; Wenger, J. C.; Baltensperger, U.; Rudich, Y.; Simpson, D.; Claeys, M.; Dommen, J.; Donahue, N. M.; George, C.; Goldstein, A. H.; et al. The Formation, Properties and Impact of Secondary Organic Aerosol: Current and Emerging Issues. *Atmos. Chem. Phys.* **2009**, *9* (14), 5155−5236.

(7) Dusek, U.; Frank, G. P.; Hildebrandt, L.; Curtius, J.; Schneider, J.; Walter, S.; Chand, D.; Drewnick, F.; Hings, S.; Jung, D.; et al. Size Matters More Than Chemistry Aerosol Particles. *Science (Washington, DC, U. S.)* **2006**, *312* (5778), 1375−1378.

(8) Stanier, C. O.; Khlystov, A. Y.; Pandis, S. N. Ambient Aerosol Size Distributions and Number Concentrations Measured during the Pittsburgh Air Quality Study (PAQS). *Atmos. Environ.* **2004**, *38* (20), 3275−3284.

(9) Thamban, N. M.; Tripathi, S. N.; Moosakutty, S. P.; Kuntamukkala, P.; Kanawade, V. P. Internally Mixed Black Carbon in the Indo-Gangetic Plain and Its Effect on Absorption Enhancement. *Atmos. Res.* **2017**, *197*, 211−223.

(10) Shamjad, P. M.; Tripathi, S. N.; Thamban, N. M.; Vreeland, H. Refractive Index and Absorption Attribution of Highly Absorbing Brown Carbon Aerosols from an Urban Indian City-Kanpur. *Sci. Rep.* **2016**, *6*, 37735.

(11) Shamjad, P. M.; Tripathi, S. N.; Pathak, R.; Hallquist, M.; Arola, A.; Bergin, M. H. Contribution of Brown Carbon to Direct Radiative Forcing over the Indo-Gangetic Plain. *Environ. Sci. Technol.* **2015**, *49* (17), 10474−10481.

(12) Satish, R.; Shamjad, P.; Thamban, N.; Tripathi, S.; Rastogi, N. Temporal Characteristics of Brown Carbon over the Central Indo-Gangetic Plain. *Environ. Sci. Technol.* **2017**, *51* (12), 6765−6772.

(13) Chakraborty, A.; Bhattu, D.; Gupta, T.; Tripathi, S. N.; Canagaratna, M. R. Real-Time Measurements of Ambient Aerosols in a Polluted Indian City: Sources, Characteristics, and Processing of Organic Aerosols during Foggy and Nonfoggy Periods. *J. Geophys. Res. Atmos.* **2015**, *120* (17), 9006−9019.

(14) Nair, V. S.; Moorthy, K. K.; Alappattu, D. P.; Kunhikrishnan, P. K.; George, S.; Nair, P. R.; Babu, S. S.; Abish, B.; Satheesh, S. K.; Tripathi, S. N.; et al. Wintime Aerosol Characteristics over the Indo-Gangetic Plain (IGP): Impacts of Local Boundary Layer Processes and Long-Range Transport. *J. Geophys. Res.: Atmos.* **2007**, *112* (D13), D13205.

(15) Shamjad, P. M.; Tripathi, S. N.; Aggarwal, S. G.; Mishra, S. K.; Joshi, M.; Khan, A.; Sapra, B. K.; Ram, K. Comparison of Experimental and Modeled Absorption Enhancement by Black Carbon (BC) Cored Polydisperse Aerosols under Hygroscopic Conditions. *Environ. Sci. Technol.* **2012**, *46* (15), 8082−8089.

(16) Kumar, B.; Chakraborty, A.; Tripathi, S. N.; Bhattu, D. Highly Time Resolved Chemical Characterization of Submicron Organic Aerosols at a Polluted Urban Location. *Environ. Sci. Process. Impacts* **2016**, *18* (10), 1285−1296.

(17) Bhattu, D.; Tripathi, S. N. CCN Closure Study: Effects of Aerosol Chemical Composition and Mixing State. *J. Geophys. Res. Atmos.* **2015**, *120* (2), 766−783.

(18) Goldstein, A. H.; Worton, D. R.; Williams, B. J.; Hering, S. V.; Kreisberg, N. M.; Panić, O.; Górecki, T. Thermal Desorption Comprehensive Two-Dimensional Gas Chromatography for in-Situ Measurements of Organic Aerosols. *J. Chromatogr. A* **2008**, *1186* (1−2), 340−347.

(19) Canagaratna, M. R.; Jayne, J. T.; Jimenez, J. L.; Allan, J. D.; Alfarra, M. R.; Zhang, Q.; Onasch, T. B.; Drewnick, F.; Coe, H.; Middlebrook, A.; et al. Chemical and Microphysical Characterization of Ambient Aerosols with the Aerodyne Aerosol Mass Spectrometer. *Mass Spectrom. Rev.* **2007**, *26* (2), 185−222.

(20) DeCarlo, P. F.; Kimmel, J. R.; Trimborn, A.; Northway, M. J.; Jayne, J. T.; Aiken, A. C.; Gonin, M.; Fuhrer, K.; Horvath, T.; Docherty, K. S.; et al. Field-Deployable, High-Resolution, Time-of-Flight Aerosol Mass Spectrometer. *Anal. Chem.* **2006**, *78* (24), 8281−8289.

(21) DeCarlo, P. F.; Slowik, J. G.; Worsnop, D. R.; Davidovits, P.; Jimenez, J. L. Particle Morphology and Density Characterization by Combined Mobility and Aerodynamic Diameter Measurements. Part 1: Theory. *Aerosol Sci. Technol.* **2004**, *38* (12), 1185−1205.

(22) Zhang, Q.; Canagaratna, M. R.; Jayne, J. T.; Worsnop, D. R.; Jimenez, J.-L. Time- and Size-Resolved Chemical Composition of Submicron Particles in Pittsburgh: Implications for Aerosol Sources and Processes. *J. Geophys. Res.: Atmos.* **2005**, *110* (D7), D07S09.

(23) Zhang, Q.; Alfarra, M. R.; Worsnop, D. R.; Allan, J. D.; Coe, H.; Canagaratna, M. R.; Jimenez, J. L. Deconvolution and Quantification of Hydrocarbon-like and Oxygenated Organic Aerosols Based on Aerosol Mass Spectrometry. *Environ. Sci. Technol.* **2005**, *39* (13), 4938−4952.

(24) Mohr, C.; Huffman, J. A.; Cubison, M. J.; Aiken, A. C.; Docherty, K. S.; Kimmel, J. R.; Ulbrich, I. M.; Hannigan, M.; Jimenez, J. L. Characterization of Primary Organic Aerosol Emissions from Meat Cooking, Trash Burning, and Motor Vehicles with High-Resolution Aerosol Mass Spectrometry and Comparison with Ambient and Chamber Observations. *Environ. Sci. Technol.* **2009**, *43* (7), 2443−2449.

(25) Allan, J. D.; Bower, K. N.; Coe, H.; Boudries, H.; Jayne, J. T.; Canagaratna, M. R.; Millet, D. B.; Goldstein, A. H.; Quinn, P. K.; Weber, R. J.; Worsnop, D. R.; et al. Submicron Aerosol Composition at Trinidad Head, California, during ITCT 2K2: Its Relationship with Gas

Phase Volatile Organic Carbon and Assessment of Instrument Performance. *J. Geophys. Res.: Atmos.* **2004**, *109* (D23), D23S24.

(26) Stephens, M.; Turner, N.; Sandberg, J. Particle Identification by Laser-Induced Incandescence in a Solid-State Laser Cavity. *Appl. Opt.* **2003**, *42* (19), 3726.

(27) Moteki, N.; Kondo, Y. Effects of Mixing State on Black Carbon Measurements by Laser-Induced Incandescence. *Aerosol Sci. Technol.* **2007**, *41* (4), 398–417.

(28) Moteki, N.; Kondo, Y. Dependence of Laser-Induced Incandescence on Physical Properties of Black Carbon Aerosols: Measurements and Theoretical Interpretation. *Aerosol Sci. Technol.* **2010**, *44* (8), 663–675.

(29) Schwarz, J. P.; Gao, R. S.; Fahey, D. W.; Thomson, D. S.; Watts, L. A.; Wilson, J. C.; Reeves, J. M.; Darbeheshti, M.; Baumgardner, D. G.; Kok, G. L.; et al. Single-Particle Measurements of Midlatitude Black Carbon and Light-Scattering Aerosols from the Boundary Layer to the Lower Stratosphere. *J. Geophys. Res.* **2006**, *111* (D16), D16207.

(30) Allan, J. D.; Jimenez, J. L.; Williams, P. I.; Alfarra, M. R.; Bower, K. N.; Jayne, J. T.; Coe, H.; Worsnop, D. R. Quantitative Sampling Using an Aerodyne Aerosol Mass Spectrometer 1. Techniques of Data Interpretation and Error Analysis. *J. Geophys. Res.: Atmos.* **2003**, *108* (D3), 4090.

(31) Alfarra, M. R.; Prevot, A. S. H.; Szidat, S.; Sandradewi, J.; Weimer, S.; Lanz, V. A.; Schreiber, D.; Mohr, M.; Baltensperger, U. Identification of the Mass Spectral Signature of Organic Aerosols from Wood Burning Emissions. *Environ. Sci. Technol.* **2007**, *41* (16), 5770–5777.

(32) Aiken, A. C.; Salcedo, D.; Cubison, M. J.; Huffman, J. A.; Decarlo, P. F.; Ulbrich, I. M.; Docherty, K. S.; Sueper, D.; Kimmel, J. R.; Worsnop, D. R.; et al. Mexico City Aerosol Analysis during MILAGRO Using High Resolution Aerosol Mass Spectrometry at the Urban Supersite (T0) ? Part 1: Fine Particle Composition and Organic Source Apportionment. *Atmos. Chem. Phys.* **2009**, *9* (17), 6633–6653.

(33) Aiken, A. C.; Decarlo, P. F.; Kroll, J. H.; Worsnop, D. R.; Huffman, J. A.; Docherty, K. S.; Ulbrich, I. M.; Mohr, C.; Kimmel, J. R.; Sueper, D.; et al. O/C and OM/OC Ratios of Primary, Secondary, and Ambient Organic Aerosols with High-Resolution Time-of-Flight Aerosol Mass Spectrometry. *Environ. Sci. Technol.* **2008**, *42* (12), 4478–4485.

(34) Canagaratna, M. R.; Jimenez, J. L.; Kroll, J. H.; Chen, Q.; Kessler, S. H.; Massoli, P.; Hildebrandt Ruiz, L.; Fortner, E.; Williams, L. R.; Wilson, K. R.; et al. Elemental Ratio Measurements of Organic Compounds Using Aerosol Mass Spectrometry: Characterization, Improved Calibration, and Implications. *Atmos. Chem. Phys.* **2015**, *15* (1), 253–272.

(35) Liu, P. S. K.; Deng, R.; Smith, K. A.; Williams, L. R.; Jayne, J. T.; Canagaratna, M. R.; Moore, K.; Onasch, T. B.; Worsnop, D. R.; Deshler, T. Transmission Efficiency of an Aerodynamic Focusing Lens System: Comparison of Model Calculations and Laboratory Measurements for the Aerodyne Aerosol Mass Spectrometer. *Aerosol Sci. Technol.* **2007**, *41* (8), 721–733.

(36) Paatero, P.; Tapper, U. Positive Matrix Factorization: A Non-Negative Factor Model with Optimal Utilization of Error Estimates of Data Values. *Environmetrics* **1994**, *5* (2), 111–126.

(37) Ulbrich, I. M.; Canagaratna, M. R.; Zhang, Q.; Worsnop, D. R.; Jimenez, J. L. Interpretation of Organic Components from Positive Matrix Factorization of Aerosol Mass Spectrometric Data. *Atmos. Chem. Phys.* **2009**, *9*, 2891–2918.

(38) Weimer, S.; Alfarra, M. R.; Schreiber, D.; Mohr, M.; Prévôt, A. S. H.; Baltensperger, U. Organic Aerosol Mass Spectral Signatures from Wood-Burning Emissions: Influence of Burning Conditions and Wood Type. *J. Geophys. Res.: Atmos.* **2008**, *113* (D10), D10304.

(39) Lanz, V. A.; Alfarra, M. R.; Baltensperger, U.; Buchmann, B.; Hueglin, C.; Szidat, S.; Wehrli, M. N.; Wacker, L.; Weimer, S.; Caseiro, A.; et al. Source Attribution of Submicron Organic Aerosols during Wintertime Inversions by Advanced Factor Analysis of Aerosol Mass Spectra. *Environ. Sci. Technol.* **2008**, *42* (1), 214–220.

(40) Ng, N. L.; Canagaratna, M. R.; Zhang, Q.; Jimenez, J. L.; Tian, J.; Ulbrich, I. M.; Kroll, J. H.; Docherty, K. S.; Chhabra, P. S.; Bahreini, R.; et al. Organic Aerosol Components Observed in Northern Hemi-spheric Datasets from Aerosol Mass Spectrometry. *Atmos. Chem. Phys.* **2010**, *10* (10), 4625–4641.

(41) DeCarlo, P. F.; Dunlea, E. J.; Kimmel, J. R.; Aiken, A. C.; Sueper, D.; Crounse, J.; Wennberg, P. O.; Emmons, L.; Shinozuka, Y.; Clarke, A.; et al. Fast Airborne Aerosol Size and Chemistry Measurements above Mexico City and Central Mexico during the MILAGRO Campaign. *Atmos. Chem. Phys.* **2008**, *8* (14), 4027–4048.

(42) Bhattu, D.; Tripathi, S. N. Inter-Seasonal Variability in Size-Resolved CCN Properties at Kanpur, India. *Atmos. Environ.* **2014**, *85*, 161–168.

(43) Decarlo, P. F.; Ulbrich, I. M.; Crounse, J.; De Foy, B.; Dunlea, E. J.; Aiken, A. C.; Knapp, D.; Weinheimer, A. J.; Campos, T.; Wennberg, P. O.; et al. Investigation of the Sources and Processing of Organic Aerosol over the Central Mexican Plateau from Aircraft Measurements during MILAGRO. *Atmos. Chem. Phys.* **2010**, *10* (12), 5257–5280.

(44) Mohr, C.; DeCarlo, P. F.; Heringa, M. F.; Chirico, R.; Slowik, J. G.; Richter, R.; Reche, C.; Alastuey, A.; Querol, X.; Seco, R.; et al. Identification and Quantification of Organic Aerosol from Cooking and Other Sources in Barcelona Using Aerosol Mass Spectrometer Data. *Atmos. Chem. Phys.* **2012**, *12* (4), 1649–1665.

(45) Zhang, Q.; Worsnop, D. R.; Canagaratna, M. R.; Jimenez, J. L. Hydrocarbon-like and Oxygenated Organic Aerosols in Pittsburgh: Insights into Sources and Processes of Organic Aerosols. *Atmos. Chem. Phys.* **2005**, *5* (12), 3289–3311.

(46) He, L.-Y.; Huang, X.-F.; Xue, L.; Hu, M.; Lin, Y.; Zheng, J.; Zhang, R.; Zhang, Y.-H. Submicron Aerosol Analysis and Organic Source Apportionment in an Urban Atmosphere in Pearl River Delta of China Using High-Resolution Aerosol Mass Spectrometry. *J. Geophys. Res.* **2011**, *116* (D12), D12304.

(47) Goetz, J. D.; Giordano, M. R.; Stockwell, C. E.; Christian, T. J.; Maharjan, R.; Adhikari, S.; Bhave, P. V.; Praveen, P. S.; Panday, A. K.; Jayarathne, T.; et al. Speciated Online PM1 from South Asian Combustion Sources − Part 1: Fuel-Based Emission Factors and Size Distributions. *Atmos. Chem. Phys.* **2018**, *18* (19), 14653–14679.

(48) Canagaratna, M. R.; Jayne, J. T.; Ghertner, D. A.; Herndon, S.; Shi, Q.; Jimenez, J. L.; Silva, P. J.; Williams, P.; Lanni, T.; Drewnick, F.; et al. Chase Studies of Particulate Emissions from In-Use New York City Vehicles. *Aerosol Sci. Technol.* **2004**, *38* (6), 555–573.

(49) Chien, S. M.; Huang, Y. J. Sizes and Polycyclic Aromatic Hydrocarbon Composition Distributions of Nano, Ultrafine, Fine, and Coarse Particulates Emitted from a Four-Stroke Motorcycle. *J. Environ. Sci. Health, Part A: Toxic/Hazard. Subst. Environ. Eng.* **2010**, *45* (13), 1768–1774.

(50) Slowik, J. G.; Cross, E. S.; Han, J. H.; Kolucki, J.; Davidovits, P.; Williams, L. R.; Onasch, T. B.; Jayne, J. T.; Kolb, C. E.; Worsnop, D. R. Measurements of Morphology Changes of Fractal Soot Particles Using Coating and Denuding Experiments: Implications for Optical Absorption and Atmospheric Lifetime. *Aerosol Sci. Technol.* **2007**, *41* (8), 734–750.

(51) Kanawade, V. P.; Tripathi, S. N.; Siingh, D.; Gautam, A. S.; Srivastava, A. K.; Kamra, A. K.; Soni, V. K.; Sethi, V. Observations of New Particle Formation at Two Distinct Indian Subcontinental Urban Locations. *Atmos. Environ.* **2014**, *96*, 370–379.

(52) Kulmala, M.; Petäjä, T.; Mönkkönen, P.; Koponen, I. K.; Dal Maso, M.; Aalto, P. P.; Lehtinen, K. E. J.; Kerminen, V.-M. On the Growth of Nucleation Mode Particles: Source Rates of Condensable Vapor in Polluted and Clean Environments. *Atmos. Chem. Phys.* **2005**, *5* (2), 409–416.

(53) Mönkkönen, P.; Koponen, I. K.; Lehtinen, K. E. J.; Hämeri, K.; Uma, R.; Kulmala, M. Measurements in a Highly Polluted Asian Mega City: Observations of Aerosol Number Size Distribution, Modal Parameters and Nucleation Events. *Atmos. Chem. Phys.* **2005**, *5* (1), 57–66.

(54) Chu, B.; Kerminen, V.-M.; Bianchi, F.; Yan, C.; Petäjä, T.; Kulmala, M. Atmospheric New Particle Formation in China. *Atmos. Chem. Phys.* **2019**, *19* (1), 115–138.

(55) Pirjola, L.; Kulmala, M.; Wilck, M.; Bischoff, A.; Stratmann, F.; Otto, E. A. Formation of Sulphuric Acid Aerosols and Cloud

Condensation Nuclei: An Expression for Significant Nucleation and Model Comparison. *J. Aerosol Sci.* **1999**, *30* (8), 1079−1094.

(56) Kulmala, M.; Maso, M. D.; Mäkelä, J. M.; Pirjola, L.; Väkevä, M.; Aalto, P.; Miikkulainen, P.; Hämeri, K.; O'Dowd, C. D. On the Formation, Growth and Composition of Nucleation Mode Particles. *Tellus, Ser. B* **2001**, *53* (4), 479−490.

(57) Salcedo, D.; Onasch, T. B.; Dzepina, K.; Canagaratna, M. R.; Zhang, Q.; Huffman, J. A.; Decarlo, P. F.; Jayne, J. T.; Mortimer, P.; Worsnop, D. R. Characterization of Ambient Aerosols in Mexico City during the MCMA-2003 Campaign with Aerosol Mass Spectrometry: Results from the CENICA Supersite. *Atmos. Chem. Phys.* **2006**, *6*, 925−946.

(58) Yang, X.; Wang, T.; Xia, M.; Gao, X.; Li, Q.; Zhang, N.; Gao, Y.; Lee, S.; Wang, X.; Xue, L.; et al. Abundance and Origin of Fine Particulate Chloride in Continental China. *Sci. Total Environ.* **2018**, *624*, 1041−1051.

(59) Stockwell, C. E.; Christian, T. J.; Goetz, J. D.; Jayarathne, T.; Bhave, P. V.; Praveen, P. S.; Adhikari, S.; Maharjan, R.; DeCarlo, P. F.; Stone, E. A.; et al. Nepal Ambient Monitoring and Source Testing Experiment (NAMaSTE): Emissions of Trace Gases and Light-Absorbing Carbon from Wood and Dung Cooking Fires, Garbage and Crop Residue Burning, Brick Kilns, and Other Sources. *Atmos. Chem. Phys.* **2016**, *16* (17), 11043−11081.